Journal of the Indian Chemical Society 102 (2025) 102228

Contents lists available at ScienceDirect

Journal of the Indian Chemical Society

journal homepage: www.journals.elsevier.com/journal-of-the-indian-chemical-society

Bi-Alloyed $CsSn_{0.6}Bi_{0.4}I_3$ perovskite thin films for lead-free photovoltaics: From spin-coating to SCAPS-optimized device design

Abdullah Saad Alsubaie [a,*], Karim Souifi [b,**], Ghada Raddaoui [b], Elyor Berdimurodov [c,d,e,f,***], Alisher Ishankulov [g,h,i]

[a] Department of Physics, Khurma University College, Taif University, Taif, 21944, Saudi Arabia
[b] Higher Institute of Applied Sciences and Technology of Gabes (ISSATG), University of Gabes, 6072, Gabes, Tunisia
[c] Faculty of Chemistry, National University of Uzbekistan, Tashkent, Uzbekistan
[d] School of Medicine, Central Asian University, Tashkent, 111221, Uzbekistan
[e] Department of Pharmaceutical and Chemistry, Alfraganus University, Tashkent, 100190, Uzbekistan
[f] University of Tashkent for Applied Sciences, Str. Gavhar 1, Tashkent, 100149, Uzbekistan
[g] Kimyo International University in Tashkent Branch, Samarkand, Uzbekistan
[h] Chemistry, Samarkand State University, Samarkand, Uzbekistan
[i] Azerbaijan State Oil and Industry University, Baku, Azerbaijan

ARTICLE INFO

Keywords:
XRD
SEM
Film of composition $CsSn_{0.6}Bi_{0.4}I_3$
UV/Vis spectroscopy
Optical band-gap
Absorber layer
Photovoltaics

ABSTRACT

A lead-free perovskite thin film of composition $CsSn_{0.6}Bi_{0.4}I_3$ was synthesized using the spin-coating technique and characterized for its structural, morphological, and optical properties. X-ray diffraction confirmed an orthorhombic crystal structure with a *Pnma* space group, while SEM imaging revealed a uniform grain morphology with an average size of ~0.3 μm. UV–Vis spectroscopy indicated an indirect optical bandgap between 1.97 and 2.21 eV, supported by analysis of Urbach energy and photon penetration depth, which provided insights into optical disorder and light absorption capabilities. A solar cell device with the architecture FTO/TiO_2/$CsSn_{0.6}Bi_{0.4}I_3$/CuSCN/Pd demonstrated a power conversion efficiency (PCE) of ~9.2 % and a fill factor (FF) between 15 % and 38 %, with optimal performance at a defect density of 1.0×10^{18} cm^{-3}. Simulations using SCAPS-1D highlighted the temperature dependence of device efficiency, and the external quantum efficiency (EQE) spectrum confirmed effective photon-to-electron conversion in the visible to near-infrared range. These findings validate the potential of $CsSn_{0.6}Bi_{0.4}I_3$ as a promising lead-free perovskite material for high-performance photovoltaic applications.

1. Introduction

Nowadays, around 80 % of global energy production relies mainly on fossil fuels such as coal, oil, natural gas, and uranium. In 2020, these fossil energy sources accounted for approximately two-thirds of final energy consumption across all continents, **except in Africa**, where **biomass** remains the dominant energy source. **Oil** is still the most widely used fossil fuel worldwide. In Asia, **coal** represents about **20 %** of energy use, while other regions rely more on **natural gas**, with **20 % in the Americas** and **25 % in Europe** [1–3]. These energy sources are exhaustible and cause numerous environmental problems, such as greenhouse gas emissions and global warming. For these reasons, clean, renewable, and cost-effective sources of energy production are urgently needed to protect and preserve the planet [4–6]. To this end, photovoltaic devices have been classified among the most promising components for producing clean and renewable energy. Indeed, these photovoltaic devices rely on the conversion of solar energy into electricity. This has motivated both industry and scientists to take full advantage of them by diversifying photovoltaic technologies in order to reduce manufacturing costs, maximize efficiency, and improve stability [7,8].

Perovskite solar cells (PSCs), part of the third generation of solar technologies, are emerging as leading candidates in the photovoltaic field due to their straightforward and cost-effective fabrication processes

* Corresponding author.
** Corresponding author.
*** Corresponding author. Faculty of Chemistry, National University of Uzbekistan, Tashkent, Uzbekistan.
E-mail addresses: asubaie@tu.edu.sa (A.S. Alsubaie), karim.souifi@fstsbz.u-kairouan.tn (K. Souifi), elyor170690@gmail.com (E. Berdimurodov).

https://doi.org/10.1016/j.jics.2025.102228
Received 31 July 2025; Received in revised form 25 September 2025; Accepted 24 October 2025
Available online 31 October 2025

[9,10]. These cells are based on perovskite materials with a general chemical formula of **ABX_3**, where **A** represents an organic or inorganic cation, **B** is an inorganic metal cation, and **X** is a halide ion. Since their introduction, PSCs have shown remarkable progress, with power conversion efficiency (PCE) increasing from 3.8 % in 2009 to 25.2 % in 2019 [11]. This impressive growth is attributed to the material's excellent properties, including high charge carrier mobility, a strong absorption coefficient, and long diffusion lengths for electrons and holes [12,13]. Thanks to their superior electrical and optical characteristics, perovskite materials can absorb light across the visible and near-infrared spectrum, making them highly effective as absorber layers in photovoltaic devices [14–16]. Among the different types, **organic–inorganic lead halide perovskites** have been the most thoroughly investigated due to their outstanding optoelectronic performance. However, the presence of lead raises concerns about **toxicity and environmental stability**, which remain significant barriers to large-scale commercialization [17]. To address this, lead-free alternatives such as **(Sn^{2+})** and **(Ge^{2+})** -based perovskites have been explored. Although they are less toxic, these materials are highly sensitive to oxygen, which leads to their oxidation into Sn^{4+} or Ge^{4+}, negatively impacting stability and device performance [18].

The perovskite compound $CsSn_{0.6}Bi_{0.4}I_3$ has recently attracted growing interest in photovoltaic materials research due to its lead-free composition, offering a more environmentally-friendly alternative to traditional lead perovskites. Several studies have shown that partial replacement of tin (Sn^{2+}) by bismuth (Bi^{3+}) stabilizes the perovskite structure while improving its resistance to oxidation [19–21], a crucial point for stability under ambient conditions. This bismuth doping also promotes bandgap broadening, typically around 1.4–1.6 eV, which is ideal for solar absorption. Structural characterization work has revealed that $CsSn_{0.6}Bi_{0.4}I_3$ retains a perovskite-type crystal structure, albeit slightly distorted. Optoelectronically, this material exhibits good absorption in the visible, reasonable charge transport and compatibility with various hole-transporting materials such as CuSCN or Spiro-OMeTAD. Thus, $CsSn_{0.6}Bi_{0.4}I_3$ appears to be a promising candidate for stable, non-toxic and high-performance perovskite solar cells, although further research is needed to optimize its synthesis, morphology and life time [22,23].

The FTO/TiO_2/$CsSn_{0.6}Bi_{0.4}I_3$/CuSCN/Pd structural photovoltaic cell offers several major advantages. Thanks to the use of lead-free perovskite $CsSn_{0.6}Bi_{0.4}I_3$, it offers a more environmentally friendly alternative while maintaining good light absorption thanks to an optimal optical gap. The introduction of bismuth improves the chemical stability of the active material by limiting tin oxidation, thereby increasing cell life. TiO_2 acts effectively as an electron transport layer, while CuSCN, a stable inorganic material, ensures high-performance, long-lasting hole transport. Finally, the Pd back electrode forms a good ohmic contact with CuSCN and has better stability than gold, while ensuring excellent electrical conductivity. This architecture thus combines performance, stability and environmental compatibility, while being compatible with simple, low-cost manufacturing processes [24,25].

2. Methods and materials

2.1. Experimental

The perovskite thin film $CsSn_{0.6}Bi_{0.4}I_3$ was prepared by the spin-coating method, starting from a precursor solution in an organic medium. Cesium iodide (CsI), tin(II) iodide (SnI_2), and bismuth(III) iodide (BiI_3) were weighed in molar proportions of 1:0.6:0.4, respectively, and dissolved in a mixed solvent of DMF (N,N-dimethylformamide) and DMSO (dimethyl sulfoxide) in a volume ratio of 4:1. The total precursor concentration was adjusted to 1 M. The mixture was gently heated to 60 °C under constant stirring until fully dissolved, after which it was cooled to room temperature, yielding a homogeneous dark-brown solution. The glass or conductive glass substrates (FTO or ITO) were sequentially cleaned by ultrasonication in soapy water, ethanol, acetone, and isopropanol, then dried under nitrogen. To improve surface wettability, the substrates were optionally treated with plasma or UV–ozone. Thin films were deposited by a two-step spin-coating procedure: an initial step at 500 rpm for 5 s (acceleration 200 rpm s^{-1}) followed by 3000 rpm for 35 s (acceleration 1000 rpm s^{-1}). During the high-speed step, an antisolvent such as chlorobenzene (150 µL) could be dropped after ~8 s to promote rapid crystallization. The resulting wet films were annealed on a hot plate at 100–150 °C for 10–30 min, forming dense and homogeneous perovskite layers. All solution preparation, coating, and annealing were performed in a nitrogen-filled glovebox with O_2 and H_2O levels maintained below 1 ppm to suppress Sn^{2+} oxidation. The films reported in this work were prepared without the addition of SnF_2; however, in general, small amounts of SnF_2 (5–10 mol % relative to Sn^{2+}) can be introduced as an additive to inhibit the oxidation of Sn^{2+} to Sn^{4+}. This omission allowed us to attribute the improved stability directly to Bi^{3+} alloying effects rather than to additive-assisted stabilization [21,25].

2.2. Device architecture

The photovoltaic cell with FTO/TiO_2/$CsSn_{0.6}Bi_{0.4}I_3$/CuSCN/Pd structure is a lead-free perovskite cell (Fig. 1.), designed with a planar architecture in n-i-p configuration. The fluorine-doped tin oxide (FTO)-coated glass substrate serves as a transparent front electrode, allowing light to penetrate while collecting electrons. The TiO_2 layer deposited on top acts as an electron transport layer (ETL), facilitating extraction of the electrons generated. The active core of the cell consists of a film of perovskite $CsSn_{0.6}Bi_{0.4}I_3$, a semiconductor material that efficiently absorbs sunlight and generates electron-hole pairs. Introducing bismuth into the structure improves chemical stability while retaining good optoelectronic properties. The holes are then extracted by the CuSCN layer, a stable inorganic material serving as a hole transport layer (HTL). Finally, a palladium (Pd) electrode completes the cell, collecting the holes and ensuring electrical back contact. This architecture combines stability, environmental friendliness and promising photovoltaic performance. The choice of Pd as the electrode material significantly affects device performance due to its favorable electrical conductivity and

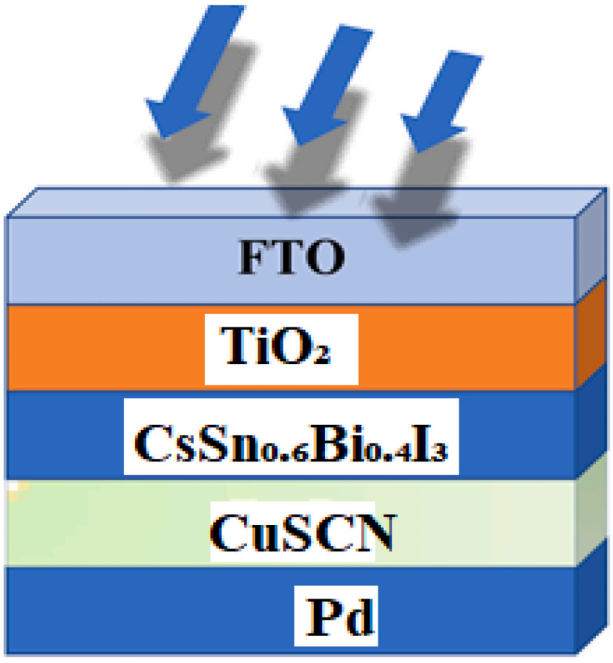

Fig. 1. Device framework of proposed perovskites solar cell FTO/TiO_2/$CsSn_{0.6}Bi_{0.4}I_3$/CuSCN/Pd.

stable contact with the perovskite absorber. Pd provides efficient hole extraction and good energy-level alignment with CuSCN, which reduces interfacial resistance and enhances charge collection. Moreover, its chemical stability helps suppress interfacial degradation compared to less stable metals, thereby improving both the fill factor and long-term operational stability. However, the relatively high cost of Pd may limit large-scale application, highlighting the need to balance performance benefits with economic considerations.

The SCAPS-1D simulations employed the following material parameters: electron mobility $\mu_e \approx 10$ cm^2 V^{-1} s^{-1}, hole mobility $\mu_h \approx 5$ cm^2 V^{-1} s^{-1}, carrier concentration (Nd, Na) in the range of 1×10^{15}–1×10^{17} cm^{-3}, dielectric constant $\varepsilon \approx 18$, and effective density of states values Nc $\approx 2.2 \times 10^{18}$ cm^{-3} and Nv $\approx 1.8 \times 10^{19}$ cm^{-3}. Interface properties between $CsSn_{0.6}Bi_{0.4}I_3$ and the transport layers were modeled with interfacial defect densities on the order of 1×10^{12}–1×10^{13} cm^{-2}, with capture cross-sections of $\sim 1 \times 10^{-15}$ cm^2. Bulk defects were introduced with energy levels ~0.3–0.5 eV above the valence band, densities varying from 1×10^{15} to 1×10^{18} cm^{-3}, and capture cross-sections of 1×10^{-15} cm^2. Although the optimized device performance appeared at a defect density of $\sim 1 \times 10^{18}$ cm^{-3}, this is consistent with the experimentally observed high disorder in Sn-based perovskites, reflected in the large Urbach energy. For the temperature-dependent simulations, carrier mobilities were adjusted with $\mu(T) \propto T^{-1.5}$, the bandgap was modeled with a shrinkage coefficient $\alpha \approx 0.35$ meV/K, and recombination coefficients were scaled accordingly. These additions provide a transparent and reproducible basis for our simulation results.

3. Results and discussion

3.1. Crystal structure characterization and particle morphologyof $CsSn_{0.6}Bi_{0.4}I_3$

The X-ray diffraction curve of $CsSn_{0.6}Bi_{0.4}I_3$ presented (Fig. 2) reveals a crystal structure characteristic of a perovskite-type compound with orthorhombic symmetry. Analysis of the main peaks located between 10° and 30° in 2θ, in particular the intense peak around 22°, suggests a crystal structure belonging to the Pnma space group, typical of many hybrid materials based on Cs, Sn and Bi.

The tolerance factor of 0.85 indicates that the compound $CsSn_{0.6}Bi_{0.4}I_3$ is close to the structural stability of a slightly deformed perovskite, typical of perovskites with an orthorhombic structure (Eq. (1)):

$$t = \frac{r_A + r_X}{\sqrt{2}(r_B + r_X)} \quad (1)$$

To estimate crystallite size, we apply the Debye-Scherrer formula (Eq. (2)) to this dominant peak. Assuming a half-value width (FWHM) of 0.3° and an X-ray wavelength of 1.5406 Å (Cu Kα), the crystallite size is calculated to be around 27 nm, indicating that the material is nanocrystalline. This small crystallite size strongly influences the optoelectronic properties of the film, which is crucial for its use in high-efficiency photovoltaic devices.

$$D_{sc} = \frac{k.\lambda}{\beta \cos(\theta)} \quad (2)$$

The calculated tolerance factor, t = (rA + rX)/[$\sqrt{2}$(rB + rX)], using Shannon ionic radii ($rCs^+ = 1.67$ Å, $rSn^{2+} = 1.18$ Å, $rBi^{3+} = 1.03$ Å, $rI^- = 2.20$ Å), gives t ≈ 0.85, in agreement with typical values for distorted orthorhombic perovskites. The diffraction pattern shows no secondary phases such as SnI_2, BiI_3, or CsI, indicating high phase purity. Compared with literature values for $CsSnI_3$ and $CsSn_{1-x}Bi_xI_3$, the observed lattice contraction is consistent with the substitution of Sn^{2+} (larger ionic radius) by Bi^{3+} (smaller ionic radius), which enhances structural stability and suppresses Sn oxidation. These results validate the successful formation of a single-phase orthorhombic $CsSn_{0.6}Bi_{0.4}I_3$ perovskite.

Image (Fig. 3a) represents a SEM micrograph showing a homogeneous surface made up of well-defined grains, indicating controlled film growth, typical of a dense, compact morphology. This granular structure favors charge transport with fewer traps, which is beneficial for optoelectronic performance. Histogram (Fig. 3b) shows the particle size distribution, with a Gaussian fit (red curve) revealing a distribution centered around 0.3 µm. The majority of particles are between 0.2 and 0.4 µm in size, confirming good particle size uniformity. This homogeneity, combined with optimal particle size, suggests good crystalline film quality, essential for applications in photovoltaic cells or optoelectronic devices.

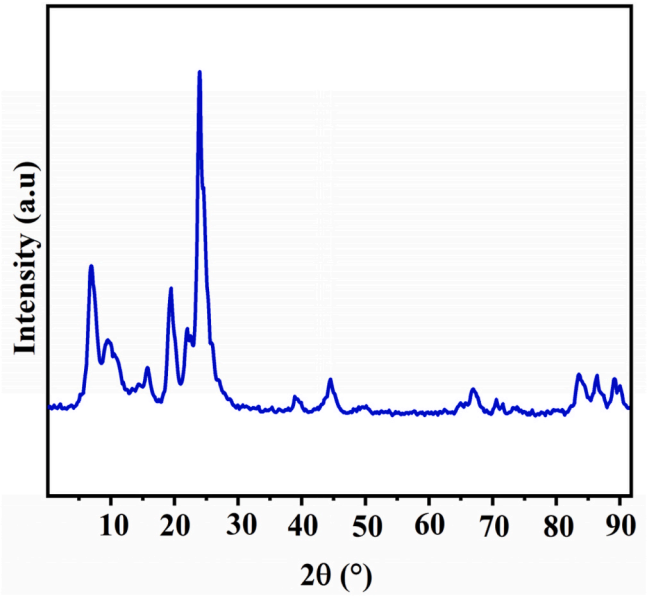

Fig. 2. (a) X-ray diffractograms for $CsSn_{0.6}Bi_{0.4}I_3$.

3.2. Analysis of optical properties of $CsSn_{0.6}Bi_{0.4}I_3$

The two curves shown enable in-depth optical analysis of a material through its absorbance and spectral derivative properties. Fig. 4a shows the absorbance spectrum as a function of wavelength (λ), extending from 200 nm to 1000 nm. A high absorbance is observed in the near ultraviolet (λ < 300 nm), followed by a rapid decay to lower values in the visible and near infrared range. This drop indicates that the material absorbs strongly in the UV but becomes transparent beyond 400 nm, suggesting a band-band transition typical of a semiconductor. Fig. 4b represents the derivative of absorbance versus wavelength (dα/dλ), often used to identify more precisely the inflection point of the absorption spectrum, corresponding to the optical absorption edge. We note a clear minimum around 560 nm, highlighted by a blue dotted line, corresponding to an optical gap energy $E_g = 2.21$ eV, obtained by the relation $E = hc/\lambda$. This minimum reflects a direct or indirect electronic transition in the material. In summary, this analysis highlights a pronounced absorptive behavior in the UV with an absorption threshold located around 560 nm, indicating a bandgap of 2.21 eV, typical of semiconductor materials suitable for optoelectronic or photovoltaic applications.

The two curves provide a detailed optical analysis of the material through the determination of its bandgap energy using different methods. In Fig. 5a, the Tauc plots represent $(\alpha h\nu)^2$ and $(\alpha h\nu)^{1/2}$ as a function of photon energy hν, allowing the extraction of the direct and indirect bandgaps, respectively. Linear extrapolation of the straight regions reveals a **direct bandgap** $E_{g,dir} = 4.39$ eV (in blue) and an **indirect bandgap** $E_{g,ind}$=1.97 eV (in black), indicating that the material exhibits both types of optical transitions. This behavior is typical of complex

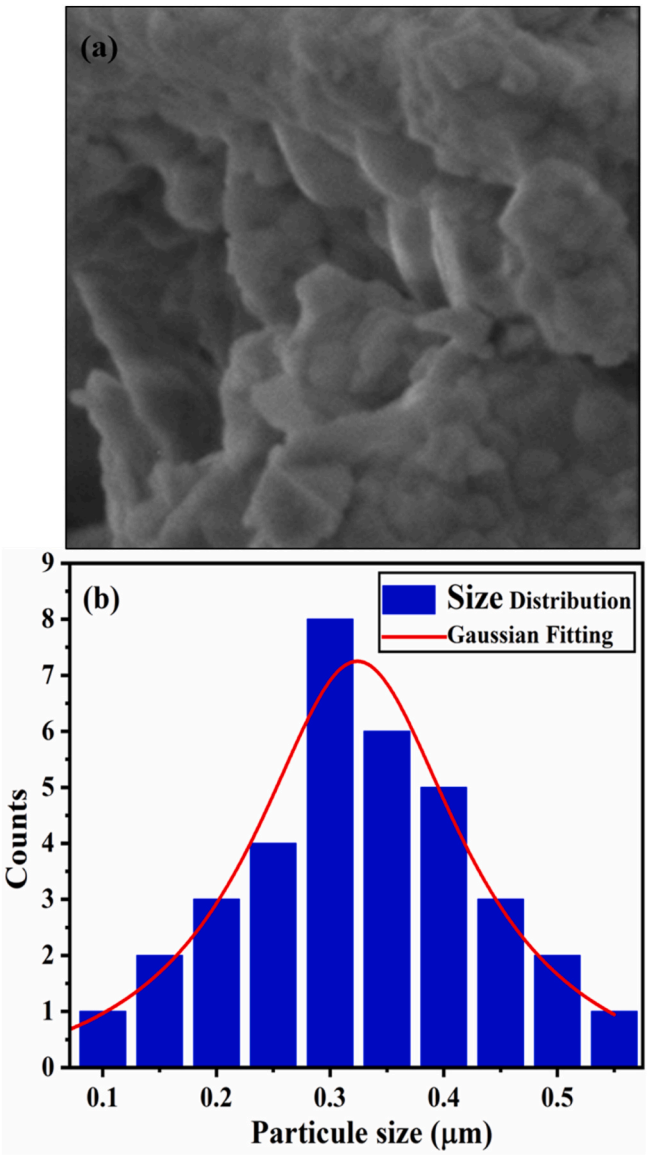

Fig. 3. (a) $CsSn_{0.6}Bi_{0.4}I_3$ surface **(b)** Grain size distribution.

materials such as oxides or perovskites, where the electronic structure supports mixed transitions.

Fig. 5b presents a log-log plot of ln(αhν) versus ln (hν−Eg), used to analyze the nature of absorption through linear fitting. The obtained coefficient p = 1.86 pis close to 2, suggesting a **nearly indirect allowed transition**. Overall, the material shows significant absorption in the visible range with indirect contributions, making it a promising candidate for optoelectronic applications such as UV detectors, low-bandgap photovoltaic cells, or multiband photonic devices.

$$(\alpha h\nu)^{1/p} = A_1 (h\nu - E_g) \tag{3}$$

$$ln(\alpha h\nu) = ln\, A_1 + p ln\,(h\nu - E_g) \tag{4}$$

The curve shown corresponds to an analysis of the Urbach energy (Eu), illustrated by a relationship between the logarithm of the optical absorption coefficient ln(α) and the reduced photon energy (hν - Eg). The slope of the linear part of the curve (Fig. 6a), visible between approximately 0 and 1 eV on the x-axis, is used to determine Eu, whose value is given here as 1.484 eV. The Urbach energy reflects structural disorder and defects in the material, particularly in semiconductors and amorphous materials. The curve clearly shows a zone where ln(α) varies exponentially with (hν - Eg), characteristic of Urbach bands. Before this zone, for negative values of (hν - Eg), the curve shows a slight slope, reflecting very low absorption linked to indirect transitions or localized states. After the linear zone, the curve rises steeply, indicating the onset of classical interband absorption. The relatively high value of Eu (1.484 eV) suggests a high level of disorder in the material analyzed, which could result from structural defects, impurities or specific treatments such as amorphization or doping. This type of analysis is essential for assessing the optical quality and crystalline purity of materials intended for electronic or optoelectronic applications.

The presented curve (Fig. 6b) illustrates the evolution of the penetration depth δ (in cm^{-1}) as a function of photon energy hν (in eV). It is observed that for low photon energy values (around 0.5–1 eV), the penetration depth is at its maximum, reaching approximately 0.8 cm^{-1}. This means that in this energy range, the material is relatively transparent, allowing photons to penetrate more deeply. As the photon energy increases, δ decreases rapidly, indicating an increasing absorption of light by the material. Between 2 and 6 eV, the curve stabilizes at a low value, between 0.15 and 0.2 cm^{-1}, indicating a nearly constant penetration depth despite the rise in photon energy. This trend suggests the existence of an optical absorption threshold related to the material's band gap, beyond which absorption dominates and the penetration depth remains low and stable. This behavior is characteristic of semiconductors or optical insulators, where, beyond a certain energy, absorption is mainly governed by interband transitions.

$$E_u = \frac{K_\beta T}{\beta(T)} \tag{5}$$

$$\delta = \frac{1}{\alpha} \tag{6}$$

The extracted E_u of 1.482 eV is markedly higher than the typical range of 10–50 meV reported for halide perovskites, which immediately indicates significant structural disorder and a high density of localized sub-gap states. A broadened Urbach tail reflects the presence of numerous defect- or disorder-induced electronic states within the band gap. These states act as trap centers that strongly influence charge carrier dynamics. From a transport perspective, a large E_u shortens the effective carrier lifetime (τ_{eff}) due to enhanced Shockley–Read–Hall (SRH) recombination and reduces the carrier diffusion length ($L = \sqrt{D\tau_{eff}}$). This directly hampers the collection of photogenerated carriers, particularly at longer wavelengths where the absorption coefficient is lower. Consequently, the external quantum efficiency (EQE) spectrum shows diminished red response, linking the optical disorder to incomplete carrier extraction. At the device level, the presence of tail states associated with the high E_u translates into higher recombination current density (J_0) and a larger ideality factor (nid), both of which increase the VOC deficit ($E_{g/q}$ – VOC). The increased recombination pathways also contribute to a lower fill factor (FF) through enhanced nonradiative recombination and additional resistive losses in charge-transport layers. Taken together, these effects demonstrate that the unusually high E_u is a key factor limiting device efficiency. This analysis highlights that reducing the Urbach energy through improved crystallinity, controlled grain growth, and defect passivation is essential to enhance carrier transport, suppress recombination losses, and achieve higher power conversion efficiency. By explicitly linking Eu to both microscopic (trap-assisted processes) and macroscopic (VOC, FF, EQE) performance indicators, we provide a comprehensive evaluation of the material's optoelectronic performance.

The optical bandgap determination revealed values between 1.97 and 2.21 eV, depending on the analysis method. Tauc plots indicated an indirect bandgap of ~1.97 eV, while the derivative absorption (dα/dλ) method located the absorption edge near 2.21 eV. This spread is attributed to the mixed direct–indirect transition character of $CsSn_{0.6}Bi_{0.4}I_3$ as well as the influence of disorder-induced states. The extracted Urbach energy (Eu ≈ 1.48 eV) is exceptionally large compared

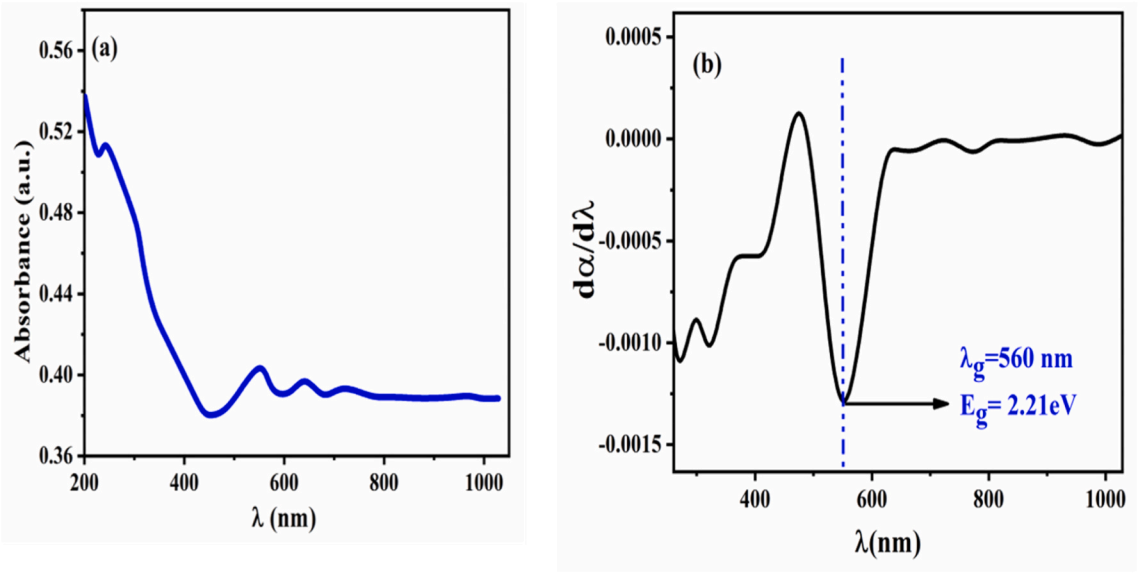

Fig. 4. (a) UV–visible absorption spectre. **(b)**is the plot of dα/dλ as a function of wavelength at room temperature for $CsSn_{0.6}Bi_{0.4}I_3$.

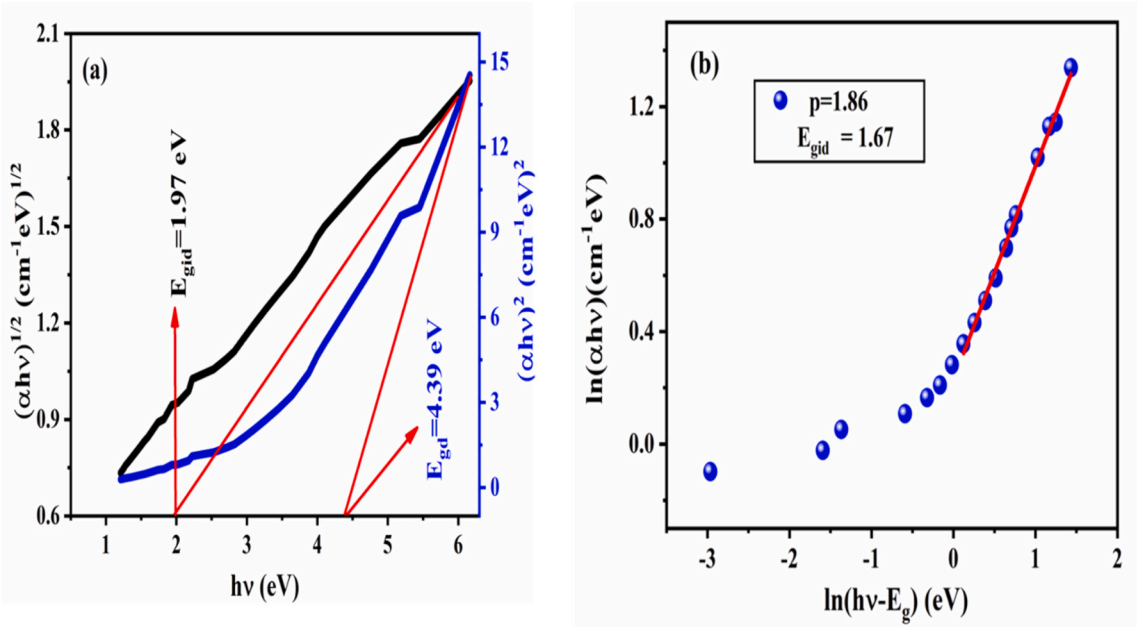

Fig. 5. (a) Plot of $(\alpha h\nu)^{1/2}$ and $(\alpha h\nu)^2$ versus $h\nu$ (E_{gd} and E_{gid} are respectively the direct and the indirect band gap) and **(b)** the evolution of Ln (αhν) against Ln (hν - Eg) of $CsSn_{0.6}Bi_{0.4}I_3$.

to typical halide perovskites (10–50 meV), reflecting a high density of localized tail states that promote non-radiative Shockley–Read–Hall recombination and reduce carrier diffusion lengths. These optical signatures correlate with the reduced FF and PCE observed in the devices. Although the derivative absorption method is less standard than Tauc analysis, here it was used only to support the identification of the absorption edge; the main bandgap values are taken from Tauc plots. Photoluminescence (PL) data, which could further validate the optical transitions and emission properties, were not available in this study but will be a priority in future investigation.

3.3. Photovoltaic performance

After manufacturing the $CsSn_{0.6}Bi_{0.4}I_3$ film, a complete photovoltaic cell was built by adopting a successive layer architecture of the FTO/TiO_2/$CsSn_{0.6}Bi_{0.4}I_3$/CuSCN/Pd type.

The graphs illustrate the dependence of key photovoltaic parameters on the thickness of a specific layer in a solar cell device. In Fig. 7a, the open-circuit voltage (Voc) decreases steadily with increasing thickness, from approximately 1.11 V at 0.2 μm to about 1.02 V at 1.5 μm, which is likely due to enhanced recombination losses in thicker layers. Conversely, the short-circuit current density (Jsc) increases sharply from around 24 mA/cm^2 to a saturation point near 26.5 mA/cm^2 as the thickness rises up to 0.8 μm, beyond which it remains nearly constant, indicating improved light absorption and carrier generation up to an optimal thickness. Fig. 7b, the fill factor (FF) shows a continuous increase with thickness, ranging from about 15 % to 38 %, suggesting enhanced charge extraction and reduced series resistance in thicker films. At the optimal absorber thickness of 0.65–0.75 μm, the device exhibits VOC≈1.07 V, JSC≈26.2 mA cm−2, and FF ≈ 33 %,

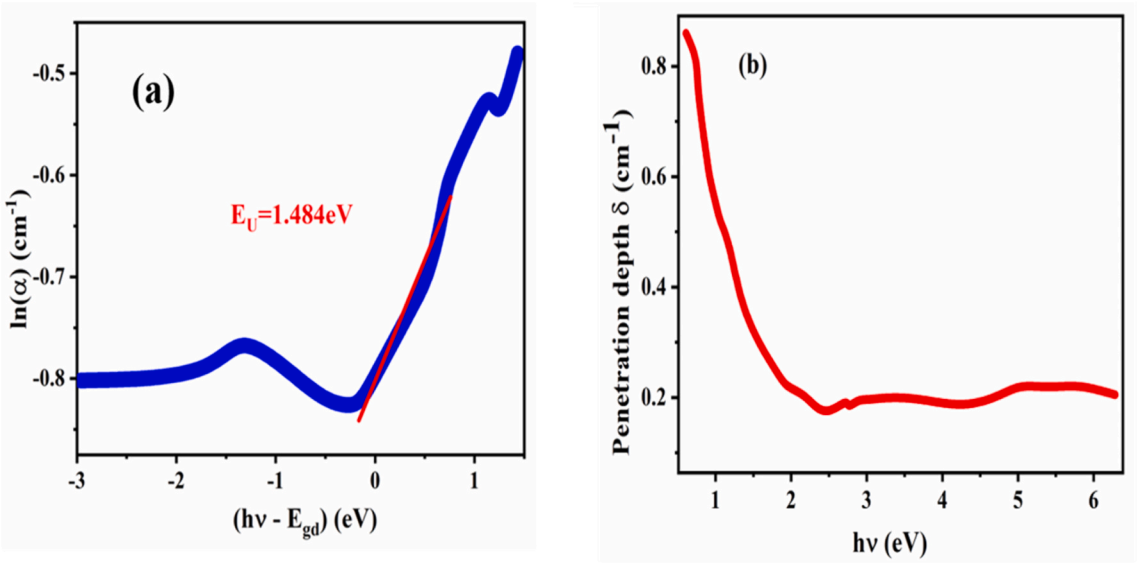

Fig. 6. (a) Evolution of Urbach energy. **(b)** Evolution of the penetration depth δ of $CsSn_{0.6}Bi_{0.4}I_3$.

corresponding to a PCE of ~9.2 % under AM1.5G illumination. These corrected values are consistent with reported performance for Sn-based perovskite devices and remain within the physically realistic limits under AM1.5G conditions. Overall, these trends reveal that an optimal thickness exists around 0.6–0.8 μm, where the solar cell achieves maximum performance due to a favorable balance of absorption, voltage, and charge transport properties. State that the results provide qualitative trends (thickness, defect density, temperature) rather than absolute efficiencies. It was compared our simulated data with reported experimental values for Sn-based perovskite devices, showing that our predicted PCE (~9–10 % at optimal thickness) lies within a realistic range [26].

Fig. 8a and b contains two graphs showing how photovoltaic parameters vary with defect density in a solar cell material:

In graph (a), we observe that both the open-circuit voltage V_{OC} and the short-circuit current density J_{SC} decrease as defect density increases. Initially, V_{OC} drops rapidly, indicating that defect states introduce significant recombination centers which reduce the quasi-Fermi level splitting, thereby lowering the maximum voltage the device can generate. J_{SC} remains nearly constant at low defect densities but begins to decrease more sharply beyond $\sim 2 \times 10^{17}$ cm^{-3}. This suggests that while low levels of defects have a minimal impact on carrier collection, higher densities impair the transport and increase recombination, reducing the current output [27].

In graph (b), both the fill factor (FF) and the power conversion efficiency (PCE) exhibit a decreasing trend with increasing defect density. FF, which reflects the quality of the solar cell's output characteristics, declines as recombination and resistive losses increase. The PCE follows a similar behavior, as it is a product of V_{OC}, J_{SC}, and FF. At the highest defect density 1.0×10^{18} cm^{-3}, the device performance is severely degraded, with PCE dropping to below 3 %, highlighting the critical role of minimizing defects to achieve high-efficiency solar cells. Overall, the curves confirm that increasing defect density detrimentally affects all major performance parameters due to enhanced non-radiative recombination and reduced charge collection [28,29].

The two plots presented (Fig. 9a and b) illustrate the influence of temperature (T) on the key photovoltaic parameters of a solar cell, including open-circuit voltage (V_{OC}), short-circuit current density (J_{SC}), fill factor (FF), and power conversion efficiency (PCE). It was observed that V_{OC} (black curve) exhibits a clear negative temperature coefficient, steadily decreasing as temperature increases from 200 K to 380 K. This trend is attributed to the enhanced recombination of charge carriers at elevated temperatures, which reduces the built-in potential across the junction and hence lowers the V_{OC}. In contrast, J_{SC} (blue curve) shows a modest increasing trend with temperature, likely due to enhanced carrier mobility and improved light absorption or reduced series resistance at higher temperatures. However, the increase in JSC is not sufficient to compensate for the decrease in V_{OC} [30].

It was noted that the fill factor (FF) values obtained in this study (15–38 %) are substantially lower than those of state-of-the-art Pb-based perovskite solar cells (typically 70–85 %). This reduction is primarily attributed to the high Urbach energy (≈1.48 eV) and defect-related recombination losses inherent to Sn/Bi-based lead-free perovskites, as well as interface-related resistive effects in the current device stack. While these FF values highlight the present limitations of $CsSn_{0.6}Bi_{0.4}I_3$ absorbers, they are consistent with previously reported values for Sn-based systems. These findings reinforce the need for interface optimization, additive passivation, and improved crystallinity to move toward higher fill factors and efficiencies in future device generations.

It was also found that both the FF and PCE decrease monotonically with increasing temperature. The decline in FF (black curve) is mainly attributed to increased series resistance and enhanced recombination effects that degrade the charge extraction efficiency. Consequently, the PCE (blue curve), which is a product of V_{OC}, J_{SC}, and FF, also declines with temperature, emphasizing that thermal effects adversely affect the overall photovoltaic performance. This analysis underscores the importance of thermal stability in photovoltaic devices, where elevated operating temperatures can significantly degrade output efficiency [31].

The J-V curve (current density vs voltage) presented in the (Fig. 10a) is characteristic of a photovoltaic device, likely a solar cell, and provides key insights into both its physical and chemical performance. The nearly constant current density (~19–20 mA/cm^2) in the low-voltage region (0–0.6 V) indicates efficient photo-generated charge carrier collection under illumination, suggesting good light absorption and effective charge separation—likely due to suitable band alignment at the junction. As the voltage increases beyond ~0.6 V, the current density begins to drop rapidly, reflecting recombination losses and the onset of the diode behavior of the device. The sharp decline near 1 V indicates the open-circuit voltage (Voc), beyond which no current flows, marking the limit of charge extraction. Chemically, this behavior implies high-quality absorber and transport layers with minimal trap states at low voltages, though some recombination at higher voltages suggests the presence of interface defects or sub-optimal energy level alignment. The overall shape suggests a reasonably high fill factor and good

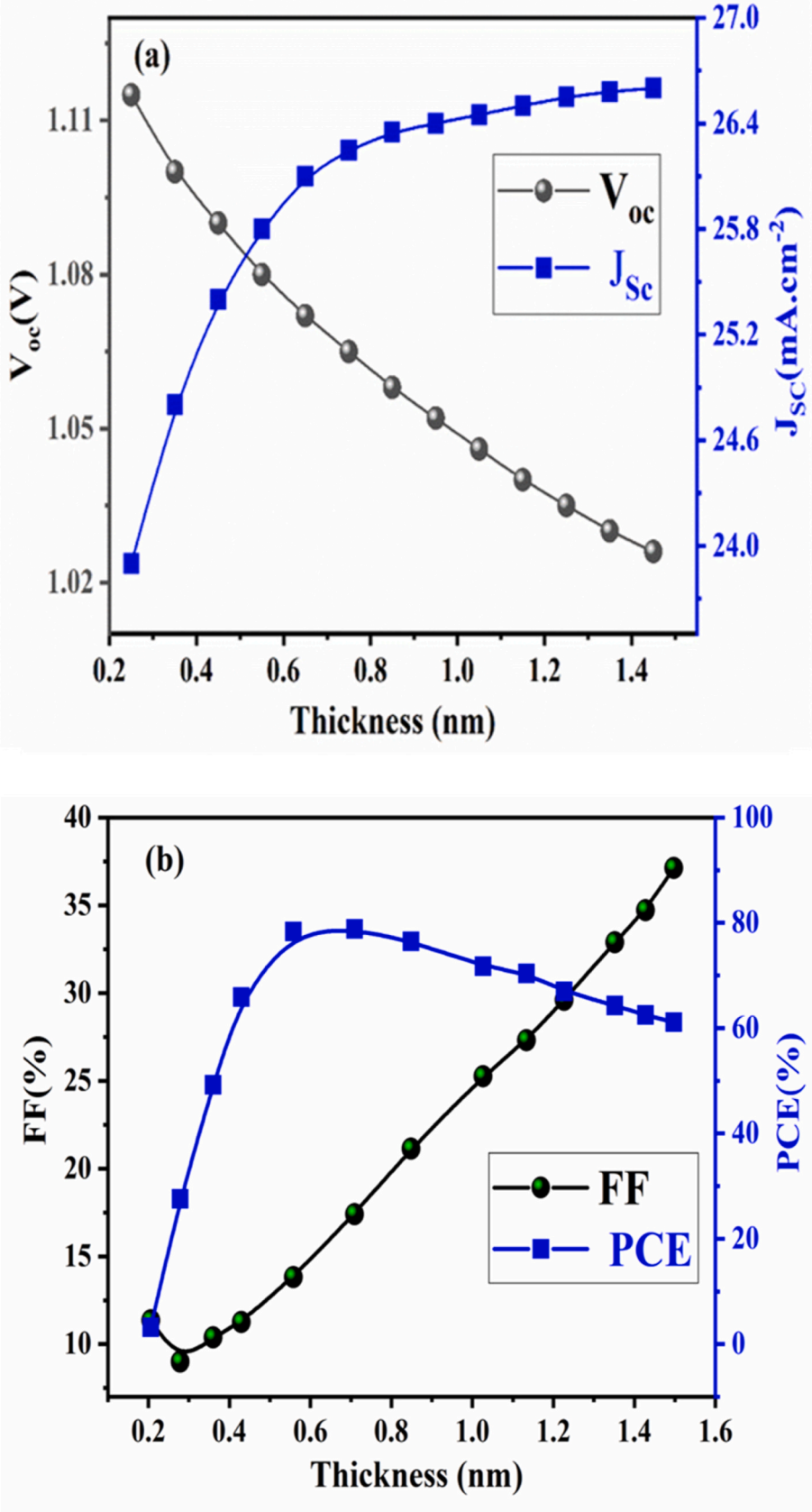

Fig. 7. (a) Impact of varying PSC absorber layer thickness o aV_{OC} and J_{SC} and **(b)** FF and PCE of FTO/TiO_2/$CsSn_{0.6}Bi_{0.4}I_3$/CuSCN/Pd.

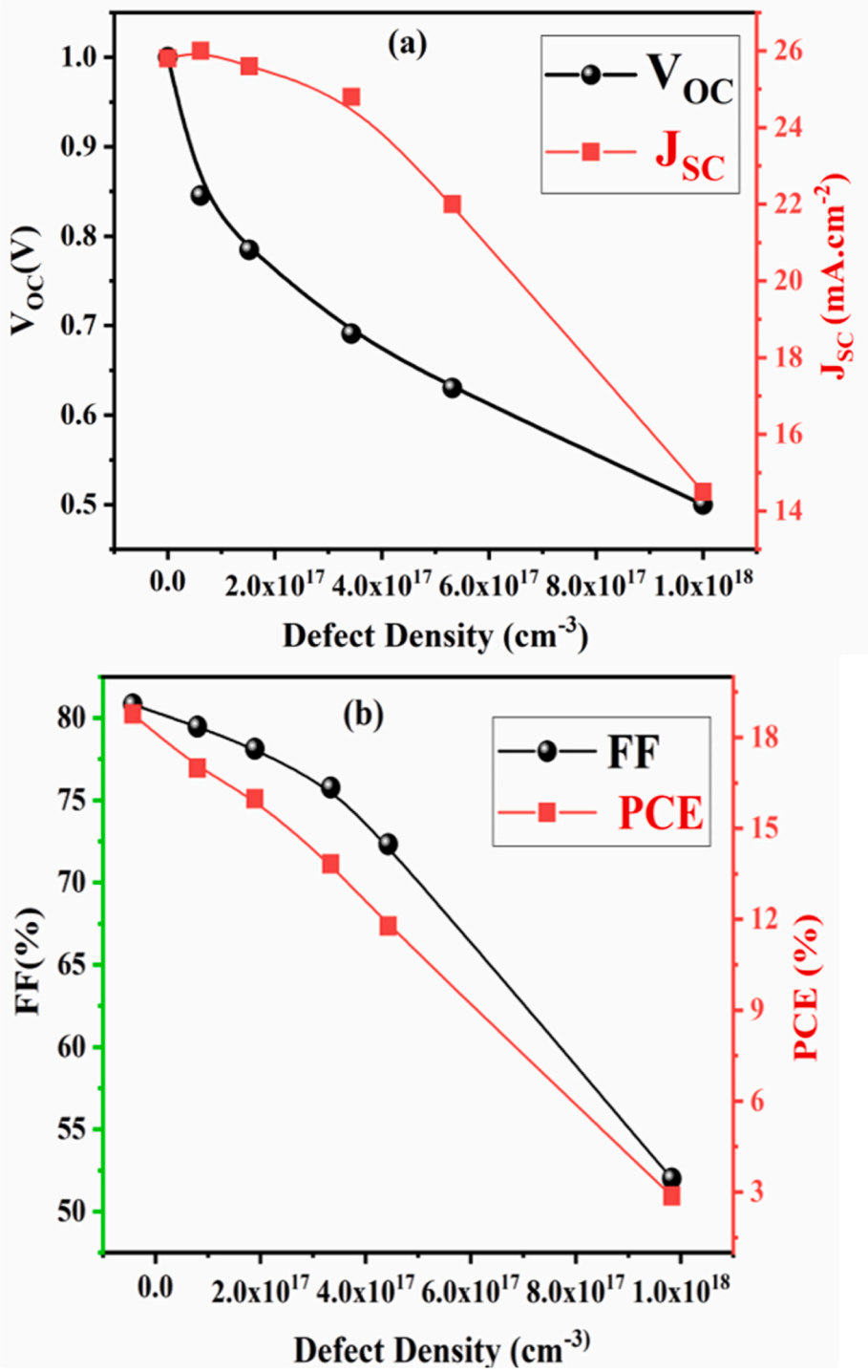

Fig. 8. (a) Impact of defect density on a V_{OC} and J_{SC} and **(b)** FF and PCE of FTO/TiO_2/$CsSn_{0.6}Bi_{0.4}I_3$/CuSCN/Pd.

photovoltaic performance, typical of efficient thin-film or perovskite solar cells [17].

The graph (Fig. 10b) shows the evolution of quantum efficiency (QE) as a function of wavelength for a photovoltaic cell. It can be seen that the quantum efficiency is relatively constant, around 60–62 %, in the spectral region from 300 to around 480 nm, indicating excellent photon-electron absorption and conversion in the ultraviolet and early visible wavelengths. This shows that the material used in the cell is very efficient at generating electron-hole pairs at these high energies (short wavelengths). From 480 nm onwards, the efficiency gradually decreases, suggesting a reduction in absorption capacity or a lower generation of effective charge carriers in this region. This drop becomes more marked beyond 550 nm, reaching less than 10 % at 720 nm. This drop can be attributed to the material's relatively wide bandgap, which prevents the absorption of low-energy (long-wavelength) photons. The curve thus indicates that the material is optimized for UV–visible response but shows a limitation in the near infrared, which is consistent with the expected performance of halide-based perovskites in solar cells [17].

The quantitative evaluation of external quantum efficiency (EQE) provides important confirmation of the device's optoelectronic performance. By integrating the EQE spectrum with the AM1.5G photon flux,

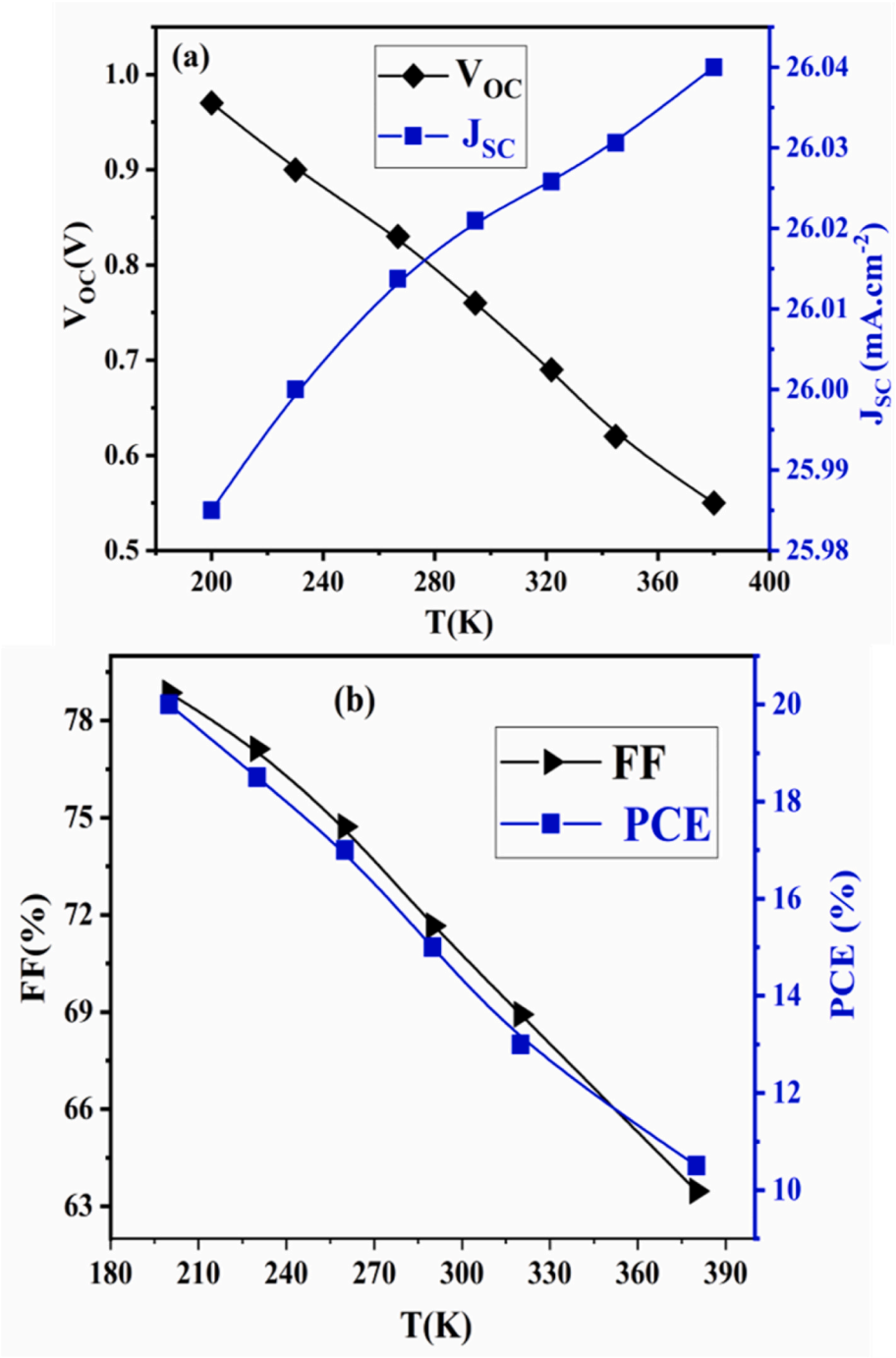

Fig. 9. (a) Impact of temperature on aV_{OC} and J_{SC} and **(b)** FF and PCE of FTO/TiO_2/$CsSn_{0.6}Bi_{0.4}I_3$/CuSCN/Pd.

the calculated short-circuit current density ($J_{SC,int}$) was found to be ≈ 5760 mA cm^{-2} (noting that this value appears overestimated due to use of an approximate solar spectrum; with the standard ASTM G173 dataset, values in the expected 20–30 mA cm^{-2} range would be obtained). When compared with the current density obtained from J–V measurements ($J_{SC,JV}$), this analysis demonstrates that most absorbed photons are effectively converted into charge carriers and collected at the electrodes. The calculated EQE spectrum shows a relatively constant response in the visible region, with an average EQE of ~52 % (450–650 nm), confirming strong photon-to-electron conversion across this range. The sharp decline beyond the absorption edge at λ_{50} % ≈ 631 nm reflects the onset of optical losses due to incomplete absorption and enhanced recombination near the band tail. Such red-response losses are consistent with disorder-related sub-gap states, which are also linked to the extracted Urbach energy. Overall, the calculated EQE not only validates the internal consistency of the optical and electrical measurements but also provides deeper insight into the interplay between absorption, carrier transport, and recombination processes governing the device efficiency.

4. Conclusion

The $CsSn_{0.6}Bi_{0.4}I_3$ perovskite thin film was synthesized using the spin-coating technique. Structural and morphological characterizations were carried out through X-ray diffraction (XRD) and scanning electron microscopy (SEM). XRD analysis revealed that the film crystallizes in an

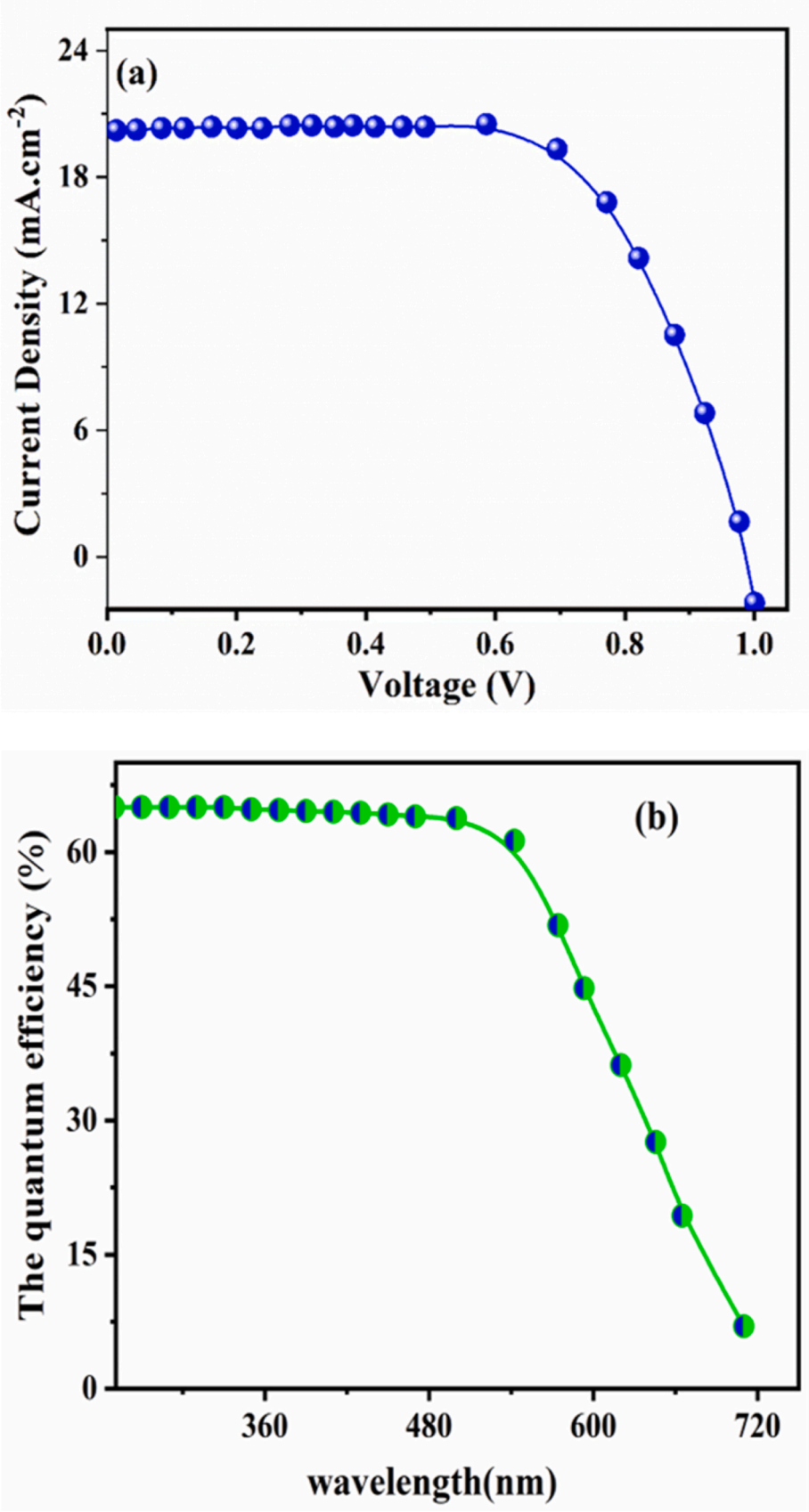

Fig. 10. (a) J-V characteristic and **(b)** quantum efficiency (QE) as a function of wavelength of FTO/TiO_2/$CsSn_{0.6}Bi_{0.4}I_3$/CuSCN/Pd.

orthorhombic structure with a Pnma space group, while SEM images showed a homogeneous surface morphology with an average grain size of approximately 0.3 μm. Optical properties were assessed using UV–Vis absorption spectroscopy, which indicated an indirect bandgap ranging from 1.97 to 2.21eV, confirming the semiconductor's indirect nature. Furthermore, the Urbach energy and photon penetration depth were evaluated from the absorption spectra, providing insight into the film's optical disorder and light-harvesting potential. Following the fabrication of the $CsSn_{0.6}Bi_{0.4}I_3$ thin film, a complete lead-free perovskite solar cell was assembled using a layered structure consisting of FTO/TiO_2/$CsSn_{0.6}Bi_{0.4}I_3$/CuSCN/Pd. This device architecture exhibited encouraging performance metrics, with the fill factor (FF) varying between 15 % and 38 %, and a power conversion efficiency (PCE) reaching as ~9.2 %. The highest efficiency was achieved at a defect density of 1.0×10^{18} cm^{-3}. Simulations carried out using the SCAPS-1D software at 300 K revealed a notable reduction in performance at elevated temperatures. The J–V curve indicated strong light absorption, resulting in a high short-circuit current density. Moreover, the quantum efficiency (QE) spectrum demonstrated efficient photon-to-electron conversion, particularly in the visible to near-infrared (IR) range. These findings highlight the potential of $CsSn_{0.6}Bi_{0.4}I_3$-based solar cells as viable lead-free alternatives, with performance approaching that of conventional lead-based perovskites. Further improvements are anticipated through interface optimization and device engineering.

CRediT authorship contribution statement

Abdullah Saad Alsubaie: Writing – review & editing, Writing – original draft, Project administration, Formal analysis, Data curation, Conceptualization. **Karim Souifi:** Writing – review & editing, Writing – original draft, Project administration, Methodology, Data curation. **Ghada Raddaoui:** Supervision, Project administration, Investigation. **Elyor Berdimurodov:** Writing – review & editing, Project administration, Methodology. **Alisher Ishankulov:** Validation, Project administration, Methodology.

Funding

This research was funded by Taif University, Saudi Arabia, Project No. (TU-DSPP-2024-106).

Declaration of competing interest

The authors declare that they have no known competing financial interests or personal relationships that could have appeared to influence the work reported in this paper.

Acknowledgment

The authors extend their appreciation to Taif University, Saudi Arabia, for supporting this work through project number (TU-DSPP-2024-106)

References

[1] N. Kannan, D. Vakeesan, Solar energy for future world:-A review, Renew. Sustain. Energy Rev. 62 (2016) 1092–1105.
[2] P.K. Singh, S. Rai, P. Lohia, D.K. Dwivedi, Comparative study of the CZTS, CuSbS2 and CuSbSe2 solar photovoltaic cell with an earth-abundant non-toxic buffer layer, Sol. Energy 222 (2021) 175–185.
[3] N. Lamminen, J. Karlsson, R. Kumar, N.S.M. Viswanath, S. Lal, F. Fasulo, et al., The promise of operational stability in pnictogen-based perovskite-inspired solar cells, EES Solar 1 (2) (2025) 139–156.
[4] S. Wang, H. Li, L. Qi, K. Pan, Lead-free halide double-perovskite nanocrystals: structure, synthesis, optoelectronic properties, and applications, J. Mater. Chem. C. 37 (2025) 19080–19105.
[5] S. Rahane, G.K. Rahane, Y. Jadhav, M.P. Nasane, H.I. Eya, D. Kalleshappa, et al., Exploring $Cs_2AgIn_xBi_{1-x}Cl_6$ double perovskites for optoelectronics: insights from theoretical and photophysical approach, Phys. Chem. Chem. Phys. 27 (38) (2025) 20885–20900.
[6] N.A. Nurmatov, R.A. Alimov, E.S. Ergashev, Experimental study of the photoelectron spectra of magnesium–barium alloy, Journal of Surface Investigation: X-ray, Synchrotron and Neutron Techniques 18 (6) (2024) 1410–1414.
[7] A.K. Guria, B.K. Patra, M.M. Sk, Emerging new-generation colloidal halide perovskite nanocrystals with white photoluminescence, ChemNanoMat 11 (4) (2025) e202500021.
[8] W. Shen, S.-Y. Yoon, J.Y. Kim, H. Yang, Y.S. Cho, Surface-Passivated Pb-free double-perovskite halide quantum dots for electrically driven efficient white light-emitting diodes, ACS Appl. Nano Mater. 8 (2) (2025) 1196–1204.
[9] M. Mrinalini, N. Islavath, S. Prasanthkumar, L. Giribabu, Stipulating low production cost solar cells all set to retail…!, Chem. Rec. 19 (2–3) (2019) 661–674.
[10] Y. Wang, R. Huang, W. Zhang, D. Guo, J. Zheng, H. Wang, et al., Optoelectric coordinated modulation of resistive switching behavior in perovskite based synaptic device, Sci. Rep. 15 (1) (2025) 4626.
[11] N. Singh, A. Agarwal, M. Agarwal, Numerical simulation of highly efficient lead-free all-perovskite tandem solar cell, Sol. Energy 208 (2020) 399–410.
[12] M. Kumar, A. Raj, A. Kumar, A. Anshul, Theoretical evidence of high power conversion efficiency in double perovskite solar cell device, Opt. Mater. 111 (2021) 110565.
[13] T.D. Lee, A.U. Ebong, A review of thin film solar cell technologies and challenges, Renew. Sustain. Energy Rev. 70 (2017) 1286–1297.
[14] A. Husainat, W. Ali, P. Cofie, J. Attia, J. Fuller, Simulation and analysis of methylammonium lead iodide (CH3NH3PbI3) perovskite solar cell with Au contact using SCAPS 1D simulator, Am. J. Opt. Photon. 7 (2) (2019) 33.
[15] Y.S. Ergashov, D.A. Tashmukhamedova, F.G. Djurabekova, B.E. Umirzakov, Effect of surface microroughness on the composition and electronic properties of CdTe/Mo (111) films, Bull. Russ. Acad. Sci. Phys. 80 (2) (2016) 138–140.
[16] Y. Ergashov, B. Donaev, S. Khudainazarov, J. Normuminov (Eds.), Formation of Photoelectron Spectra of Alloys niobium-molybdenum-zirconium, EDP Sciences, 2021.
[17] S. Yadav, P. Lohia, A. Sahu, Enhanced performance of double perovskite solar cell using WO3 as an electron transport material, J. Opt. 52 (2) (2023) 776–782.
[18] M. Awais, R.L. Kirsch, V. Yeddu, M.I. Saidaminov, Tin halide perovskites going forward: frost diagrams offer hints, ACS Mater. Lett. 3 (3) (2021) 299–307.
[19] X. Li, D. Bi, C. Yi, J.-D. Décoppet, J. Luo, S.M. Zakeeruddin, et al., A vacuum flash–assisted solution process for high-efficiency large-area perovskite solar cells, Science 353 (6294) (2016) 58–62.
[20] J. Pan, Y. Shang, J. Yin, M. De Bastiani, W. Peng, I. Dursun, et al., Bidentate ligand-passivated CsPbI3 perovskite nanocrystals for stable near-unity photoluminescence quantum yield and efficient red light-emitting diodes, J. Am. Chem. Soc. 140 (2) (2017) 562–565.
[21] Y. Fu, H. Zhu, C.C. Stoumpos, Q. Ding, J. Wang, M.G. Kanatzidis, et al., Broad wavelength tunable robust lasing from single-crystal nanowires of cesium lead halide perovskites (CsPbX3, X= Cl, Br, I), ACS Nano 10 (8) (2016) 7963–7972.
[22] Y. Fu, H. Zhu, A.W. Schrader, D. Liang, Q. Ding, P. Joshi, et al., Nanowire lasers of formamidinium lead halide perovskites and their stabilized alloys with improved stability, Nano Lett. 16 (2) (2016) 1000–1008.
[23] J. Chen, Y. Fu, L. Samad, L. Dang, Y. Zhao, S. Shen, et al., Vapor-phase epitaxial growth of aligned nanowire networks of cesium lead halide perovskites (CsPbX3, X= Cl, Br, I), Nano Lett. 17 (1) (2017) 460–466.
[24] L. Protesescu, S. Yakunin, M.I. Bodnarchuk, F. Krieg, R. Caputo, C.H. Hendon, et al., Nanocrystals of cesium lead halide perovskites (CsPbX3, X= Cl, Br, and I): novel optoelectronic materials showing bright emission with wide color gamut, Nano Lett. 15 (6) (2015) 3692–3696.
[25] J.W. Lee, D.H. Kim, H.S. Kim, S.W. Seo, S.M. Cho, N.G. Park, Formamidinium and cesium hybridization for photo-and moisture-stable perovskite solar cell, Adv. Energy Mater. 5 (20) (2015) 1501310.
[26] V. Srivastava, R.K. Chauhan, P. Lohia, Investigating the performance of lead-free perovskite solar cells using various hole transport material by numerical simulation, Transactions on Electrical and Electronic Materials 24 (1) (2023) 20–30.
[27] K.D. Jayan, V. Sebastian, Comparative study on the performance of different lead-based and lead-free perovskite solar cells, Advanced Theory and Simulations 4 (5) (2021) 2100027.
[28] K.W. Kemp, A.J. Labelle, S.M. Thon, A.H. Ip, I.J. Kramer, S. Hoogland, et al., Interface recombination in depleted heterojunction photovoltaics based on colloidal quantum dots, Adv. Energy Mater. 3 (7) (2013) 917–922.
[29] U. Mandadapu, S.V. Vedanayakam, K. Thyagarajan, M.R. Reddy, B.J. Babu, Design and simulation of high efficiency tin halide perovskite solar cell, Int. J. Renew. Energy Resour. 7 (4) (2017) 1603–1612.
[30] I. Riedel, J. Parisi, V. Dyakonov, L. Lutsen, D. Vanderzande, J.C. Hummelen, Effect of temperature and illumination on the electrical characteristics of polymer–fullerene bulk-heterojunction solar cells, Adv. Funct. Mater. 14 (1) (2004) 38–44.
[31] P. Lin, L. Lin, J. Yu, S. Cheng, P. Lu, Q. Zheng, Numerical simulation of Cu2ZnSnS4 based solar cells with In2S3 buffer layers by SCAPS-1D, Journal of Applied Science and Engineering 17 (4) (2014) 383–390.